JGR Space Physics

RESEARCH ARTICLE
10.1029/2021JA029559

Super Dual Auroral Radar Network Expansion and Its Influence on the Derived Ionospheric Convection Pattern

M.-T. Walach[1], A. Grocott[1], F. Staples[2,3], and E. G. Thomas[4]

[1]Lancaster University, Lancaster, UK, [2]Formerly at Mullard Space Science Laboratory, University College London, Dorking, UK, [3]Department of Earth, Planetary, and Space Sciences, University of California, Los Angeles, CA, USA, [4]Thayer School of Engineering, Dartmouth College, Hanover, NH, USA

Key Points:

- We identify changes in derived convection maps when PolarDARN and StormDARN are added, and show the impact of different processing
- Derived convection parameters are highly susceptible to processing variables and which radars are included
- We show how the number of backscatter echoes per map is critical to the integrity of the maps, and discuss how this impacts map quality

Supporting Information:

Supporting Information may be found in the online version of this article.

Correspondence to:

M.-T. Walach,
m.walach@lancaster.ac.uk

Citation:

Walach, M.-T., Grocott, A., Staples, F., & Thomas, E. G. (2022). Super dual auroral radar network expansion and its influence on the derived ionospheric convection pattern. *Journal of Geophysical Research: Space Physics*, *127*, e2021JA029559. https://doi.org/10.1029/2021JA029559

Received 13 MAY 2021
Accepted 12 JAN 2022

Author Contributions:

Conceptualization: M.-T. Walach, A. Grocott, F. Staples, E. G. Thomas
Data curation: M.-T. Walach
Formal analysis: M.-T. Walach, E. G. Thomas
Funding acquisition: M.-T. Walach, A. Grocott
Investigation: M.-T. Walach, A. Grocott, F. Staples
Methodology: M.-T. Walach, A. Grocott, F. Staples
Project Administration: A. Grocott
Resources: M.-T. Walach, A. Grocott
Software: M.-T. Walach
Supervision: A. Grocott

Abstract The Super Dual Auroral Radar Network (SuperDARN) was built to study ionospheric convection and has in recent years been expanded geographically. Alongside software developments, this has resulted in many different versions of the convection maps data set being available. Using data from 2012 to 2018, we produce five different versions of the widely used convection maps, using limited backscatter ranges, background models and the exclusion/inclusion of data from specific radar groups such as the StormDARN radars. This enables us to simulate how much information was missing from older SuperDARN research. We study changes in the Heppner-Maynard boundary (HMB), the cross polar cap potential (CPCP), the number of backscatter echoes (n) and the χ^2/n statistic which is a measure of the global agreement between the measured and fitted velocities. We find that the CPCP is reduced when the PolarDARN radars are introduced, but then increases again when the StormDARN radars are added. When the background model is changed from the RG96 model, to the most recent TS18 model, the CPCP tends to decrease for lower values, but tends to increase for higher values. When comparing to geomagnetic indices, we find that there is on average a linear relationship between the HMB and the geomagnetic indices, as well as n, which breaks when the HMB is located at latitudes below ~50° due to the low observational density. Whilst n is important in constraining the maps (maps with $n > 400$ data points are unlikely to differ), it is insufficient as the sole measure of quality.

Plain Language Summary The ionosphere, where space begins and the atmosphere ends, moves as a result of the Earth's magnetic field coupling with the Sun. The Super Dual Auroral Radar Network (SuperDARN) was built around the Earth's magnetic poles to study this phenomenon, known as ionospheric convection. Combining many line-of-sight convection measurements, we are able to build global maps of ionospheric convection from SuperDARN data. This encapsulates dynamics which are central to space weather phenomena. SuperDARN, which has been gathering data for decades, has over time undergone numerous transformations, including the development of new processing software and more radars being added to the network. Using data from the years 2012–2018, we perform a statistical analysis on processed SuperDARN convection maps for the entire data set and assess systematically how the data set has changed over the years. We consider how the addition of more data and differences to the convection mapping procedures can affect scientific studies in the context of this large database.

1. Introduction

The Super Dual Auroral Radar Network (SuperDARN) consists of high-frequency coherent scatter radars built to study ionospheric convection by means of Doppler-shifted, pulse sequences and has been widely used in space physics and ionospheric research (e.g., Chisham et al., 2007; Greenwald et al., 1995; Nishitani et al., 2019; Ruohoniemi & Greenwald, 1996). SuperDARN data are continuously available from 1993, with the network having expanded over time from one radar (built in 1983) to 23 radars in the Northern hemisphere, 13 in the Southern hemisphere and more under construction (Nishitani et al., 2019). This expansion has allowed for a greater area to be covered by SuperDARN (i.e., down to magnetic latitudes of 40°) with at least 16 different look directions along which each radar can sample different ranges (Nishitani et al., 2019) in the Northern hemisphere. Line-of-sight measurements by this large-scale network of radars can be combined and used to construct a picture of high-latitude ionospheric convection on time scales of 1–2 min (Ruohoniemi & Baker, 1998). The radars can be grouped into high-latitude radars (the original network), polar-latitude radars (or PolarDARN), and midlatitude radars (or StormDARN). Nishitani et al. (2019) provides a summary from a historical northern hemisphere perspective: high-latitude radars, at magnetic latitudes of 50°–70° were first built, starting in 1983 with the

Validation: M.-T. Walach
Visualization: M.-T. Walach
Writing – original draft: M.-T. Walach
Writing – review & editing: M.-T. Walach, A. Grocott, F. Staples, E. G. Thomas

Goose Bay radar, followed by the PolarDARN radars (covering 70°–90° magnetic latitude), and the expansion to mid-latitudes (∼40°–50°), starting in 2005 with the Wallops Island radar. Over time new radars have improved global ionospheric convection mapping by increasing the number of measurements and look directions.

The most commonly used SuperDARN data product by the space science and ionospheric research community is the convection maps. Convection maps are large scale maps, showing ionospheric convection around the magnetic poles. In order to produce these maps, several data processing steps have to be undertaken. Data from different radars are combined, which allows for the exclusion of data from particular radars or the specification of a range limit for the scatter. For example, slow moving E-region scatter can and should be removed by setting the minimum range gate limit to 800 km (Forsythe & Makarevich, 2017; Thomas & Shepherd, 2018). It has become apparent that far range data beyond 2,000 km may also be problematic owing to geolocation uncertainties in the range finding algorithm (Chisham et al., 2008). Once the data have been chosen and combined, a fitting algorithm is applied which fits an electrostatic potential in terms of spherical harmonic functions to the data (Ruohoniemi & Baker, 1998; Ruohoniemi & Greenwald, 1996). To find the optimal solution for the spherical harmonic coefficients, a singular value decomposition (e.g., Press et al., 2007) is minimized. When this fitting is performed, typically a background statistical convection model (hereafter referred to as just the background model), parameterized by a mix of IMF conditions and solar wind velocity depending on the model used, to infill information in the case of data gaps. This method is also known as the "Map Potential" technique. With the expansion of the radar network, as well as data processing software improvements, the resulting data product has undergone several changes.

Several models are available for the "Map Potential" method, most notably Ruohoniemi and Greenwald (1996) generated the most widely used background model, which was subsequently implemented in the RST, the Radar Software Toolkit (e.g., SuperDARN Data Analysis Working Group, Thomas, Ponomarenko, Billett, et al., 2018). This background model was thus used by most SuperDARN users when generating convection maps and used in many scientific studies. Ruohoniemi and Greenwald (1996) used data from the Goose Bay radar to derive the background statistical model. Since then however, many more radars have been added to SuperDARN. This raises the question of how much of an effect changing the background model has on the convection map data set, which was investigated by Shepherd and Ruohoniemi (2000). The main conclusion from Shepherd and Ruohoniemi (2000) was that the solution becomes insensitive to the choice of statistical model when the data coverage is high. Since then, Ruohoniemi and Greenwald (2005) produced an updated version of their background model using data from nine radars, but this was not implemented into RST, thus keeping the RG96-model the default which was used by the community. Since then, a number of updated background models, such as Pettigrew et al. (2010), Cousins and Shepherd (2010), and Thomas and Shepherd (2018) have been produced. The Pettigrew et al. (2010) and Cousins and Shepherd (2010) models were not implemented into RST until version 4.1 (SuperDARN Data Analysis Working Group, Thomas, Ponomarenko, Bland, et al., 2018). Soon after, the background model by Thomas and Shepherd (2018) was released, which is now standard in RST since version 4.2 (SuperDARN Data Analysis Working Group, Thomas, Ponomarenko, Billett, et al., 2018). The RG96 and TS18 models are thus the most widely used and we will focus our analysis on these background models.

In this paper, we conduct a large scale data analysis to assess systematically how the SuperDARN convection map data set has changed over the years and how this may have affected the derived convection maps.

We specifically probe the effects of the following changes:

1. Inclusion of the backscatter range limits
2. Addition of the PolarDARN data
3. Addition of the StormDARN data
4. Updating of the background statistical model

Comparing different versions of input data set allows for a large-scale analysis of systematic changes and in particular, how the introduction of new StormDARN and PolarDARN data modifies the convection maps on a large scale, which has implications for use of the maps in scientific studies.

In particular, we discuss measures of map quality in the context of these changes, as well as the placement of the Heppner-Maynard boundary (the lower latitude convective boundary which is used to constrain the maps).

2. Data and Method

To provide a meaningful large scale comparison of different versions of the SuperDARN data set, we process Northern hemisphere data to create different versions of the SuperDARN convection maps for the same time period (2012–2018).

To make SuperDARN convection maps we process the raw data using the Radar Software Toolkit (RST [SuperDARN Data Analysis Working Group, Thomas, Ponomarenko, Bland, et al., 2018]), which can be broken down into 5 steps:

1. Fitacf files, which include the line-of-sight velocity data, are produced from the raw radar data by applying version 2.5 of the FITACF function (SuperDARN Data Analysis Working Group et al., 2019).
2. The data from one hemisphere (in our case, the Northern hemisphere) are then gridded onto an equal area latitude-longitude grid (see Equation 1 from Ruohoniemi & Baker, 1998) and split into typically one or 2 min cadence records. The grid we use for this analysis is in the AACGM coordinate system (version 2 by Shepherd, 2014). Historically it has almost always been the case that all ionospheric data measured by the radars were added to the grids. As discussed below, we explore changing the range limit by setting the minimum range gate limit to 800 km and the far range data limit to 2,000 km.
3. A Heppner-Maynard boundary (HMB; Heppner & Maynard, 1987), the low-latitude boundary of the convection pattern where the flows approach zero, can either be specified or be chosen using backscatter measurements. This is to constrain the convection pattern when the spherical harmonic fit is applied (Shepherd & Ruohoniemi, 2000). For typical 2 min cadence convection maps, it is appropriate to find the lowest latitude where three radar velocity measurements are greater than 100 ms^{-1} to define the HMB (Imber et al., 2013). This boundary is circular around the nightside and oval-shaped on the dayside, such that it moves to higher latitudes. Previous to Shepherd and Ruohoniemi (2000), a fully circular boundary was used, which was deemed to create unrealistic flows at lower latitudes when the radar network was expanded. To make all the convection maps (D0 to D4), using RST, the HMB (Heppner & Maynard, 1987; Shepherd & Ruohoniemi, 2000) was chosen using the default method using the functional form Shepherd and Ruohoniemi (2000), using the thresholds above.
4. A background model is selected based on solar wind conditions and model vectors are added to the grid. For this, we use solar wind data from the ACE spacecraft, which has been time-lagged to the magnetosphere using the algorithm from Khan and Cowley (1999) which takes magnetosheath transit time into account. We add the model, specifying a fitting order of 6 with a "light" doping level for the background convection model, which means a minimum reliance is placed on the background model. Newer background models (Cousins & Shepherd, 2010; Pettigrew et al., 2010; Thomas & Shepherd, 2018) are all generated using a fitting order of 8, whereas Ruohoniemi and Greenwald (1996) was generated using a sixth order fit.
5. Finally, the "Map Potential" technique is applied. We use the technique from Ruohoniemi and Baker (1998) to fit electrostatic potentials to the combined measured and model velocity vectors as spherical harmonic functions.

Using the steps outlined above, we first create the data set (D0) with the high-latitude radars only, which is then modified by changing one aspect for each subsequent data set. This allows us to contrast the impact of each change in the data set. The basic data processing is the same for all the datasets, except for the differences outlined in Table 1. The specific processing commands and options used for the data processing can be found in the appendix of this paper.

Two versions of the gridded map files were created (e.g., step 2–5 is repeated) to see how changing the backscatter range limits affects the data set. One version of the gridded files was created with added backscatter range limits and one without any range limit. By only including data from a minimum range of 800 km and a maximum far range of 2,000 km, we try to eliminate all possible E-Region scatter and all backscatter with higher uncertainties in range and azimuth (i.e., projected location; Chisham et al., 2008; Forsythe & Makarevich, 2017; Thomas & Shepherd, 2018). On a statistical level, we expect this method to remove most of the data with higher uncertainty, but this method will also remove some good quality data as a substantial amount of scatter comes from ranges greater than 2,000 km. Applying these range limits may not remove all E-region scatter or all scatter with uncertain locations, but currently no better method for a large statistical data set exists. The version of gridded

Table 1
Differences Between the Comparison Datasets

Version	Introduced difference	Background model	High-latitude radars	Range limits	PolarDARN radars	StormDARN radars
D0	High-latitude radars[a] only	RG96	Yes	No	no	no
D1	Added range limits: 800–2,000 km	RG96	Yes	Yes	no	no
D2	Added PolarDARN radars[b]	RG96	Yes	Yes	yes	no
D3	Added all other (i.e., StormDARN radars)[c]	RG96	Yes	Yes	yes	yes
D4: Control set	Changed the background model	TS18	Yes	Yes	yes	yes

[a]High-latitude radars: King Salmon, Kodiak, Prince George, Saskatoon, Kapuskasing, Goose Bay, Stokkseyri, Pykkvibaer, Hankasalmi. [b]PolarDARN radars include: Inuvik, Rankin Inlet, Clyde River, Longyearbyen. [c]StormDARN radars include: Hokkaido West, Hokkaido East, Adak West, Adak East, Christmas Valley West, Christmas Valley East, Fort Hays West, Fort Hays East, Blackstone, Wallops Island.

files with backscatter range limits is used for D1-D4 and the one without a range limit is used for D0. The gridded map files were resolved into 2 min records and used the Chisham virtual height model (Chisham et al., 2008).

Data set versions D0 and D1 include the same radars, whereas for D2 and D3, more radars were included (see Table 1). For the selection of PolarDARN and StormDARN groupings the list provided by Table 1 in Thomas and Shepherd (2018) was used. The list provided in Thomas and Shepherd (2018) demonstrates that most of the StormDARN radars were built after the high-latitude and PolarDARN radars.

For D4, we keep the selection of radars the same as D3, but use the background model from Thomas and Shepherd (2018) (TS18) instead of the one from Ruohoniemi and Greenwald (1996) (RG96).

Having established this archive of 2-min resolution convection map files, we then extract a set of measured parameters with which to quantify the ionospheric convection. The HMB latitude and cross polar cap potential (CPCP) describe the spatial extent and strength of the convection and allow us to examine how changes in the processing might affect conclusions of scientific studies, whereas the number of backscatter echoes per map or the average number of backscatter points per radar allows us to study how changes affect coverage. In this study, we define the HMB latitude as the latitude of the fitted boundary on the nightside and we also investigate how this parameter changes alongside the minimum latitude where backscatter is obtained (Λ_{min}), which can be along any magnetic local time or longitude. We would thus expect the difference between the two parameters to be positive for well constrained maps (i.e., Λ_{min} is at a lower latitude than the HMB), but to be negative when either the minimum latitude of observations is on the dayside (where the HMB shifts to higher latitudes) or an indicator that the HMB is not constrained by data. We also show how the different processing affects the χ^2/n-statistic, which is often used as a global measure of map quality.

The χ^2 parameter is a result from the singular value decomposition, which is minimized when the spherical harmonic fitting is performed to find the optimal solution for the coefficients. Ruohoniemi and Baker (1998) define this as

$$\chi^2 = \sum_{i=1}^{N} \frac{1}{\sigma_i^2} \left[\mathbf{V}[i] \cdot \hat{\mathbf{k}}[i] - W_i\right]^2, \quad (1)$$

where $\boldsymbol{V}[i]$ is the fitted velocity vector at the grid cell position i, σ_i^2 is standard deviation of the fitted velocity vector at i, $\hat{k}[i]$ is the direction of the velocity vector, W_i are the uncertainties associated line-of-sight velocity uncertainties and the dot product thus provides the projection of the velocity onto the line-of-sight direction. χ^2/n was introduced by Ruohoniemi and Baker (1998) as a measure of the goodness of fit of the spherical harmonic expansion to the measured line-of-sight velocity data, where a value of 1 would indicate a good match and higher values would indicate a worse match. In this study we explore how this parameter varies and we discuss if it is an adequate measure of map quality. We discuss why χ^2/n might change and what these changes might mean for the quality of the convection maps.

Additionally, we also discuss the relationship between the HMB latitude and measures of geomagnetic activity, such as the Auroral Lower index (AL), the Auroral Electrojet index (AE) and the Symmetric Horizontal index (Sym-H, Davis & Sugiura, 1966; Iyemori, 1990). These are derived from ground-based magnetometer

measurements and are a proxy for the magnetospheric activity in response to the dayside driving and internal dynamics (Davis & Sugiura, 1966; World Data Center for Geomagnetism in Kyoto et al., 2015). We also consider the relationship between the CPCP and Φ_D, the dayside reconnection rate, which is calculated from the IMF B_{YZ} component, the solar wind speed, V_X, and IMF clock angle, θ (Milan et al., 2012; Walach et al., 2017):

$$\Phi_D = 3.3 \times 10^5 V_x^{4/3} B_{YZ} \sin^{9/2} \frac{1}{2}\theta \quad (2)$$

We compare these parameters from D0 to D3 with D4, the most modern set-up, which we use as our control data set. We compare D0 and D4 to see how the lack of a range limit, PolarDARN, StormDARN and an updated background model affects the convection maps. We compare D1 to D4 to see how the lack of PolarDARN, StormDARN and an updated background model affects the convection maps, and a D2 to D4 comparison allows us to investigate the lack of StormDARN and an updated background model affects the convection maps. Finally, a comparison between D3 to D4 allows us to see the effects on the convection maps of changing the background model only. Overall, this allows us to see which changes take us closer to the control data set, D4. The timeseries data extracted from the SuperDARN convection maps is condensed into probability distribution functions (PDF) for each parameter. Our approach allows us to further investigate how changing one parameter affects the convection maps (e.g., comparing the PDF of D1 and D4 to the PDF of D0 and D4 of the same parameter shows how adding range limits affects the data set). In Section 3.5, we also explore by how much the fitted SuperDARN velocities can increase after adding StormDARN. In the following section, we show the PDFs, which enable us to compare the effects of changing the data set on each parameter in turn. A selection of example convection maps, that illustrates some of the differences that result from changing the datasets, are shown in Figure S1.

3. Results

This section shows the probability distribution functions for the parameters discussed above. We compare the results from each data set with the control data set (D4) and discuss the parameters in turn.

3.1. The Heppner-Maynard Boundary

Figure 1 shows the probability distribution functions comparing the HMB latitude between models with the difference between the HMB latitude and Λ_{min}. The occurrences of the example maps in Figure S1 are indicated in the probability distribution functions by the light blue crosses (and green square for comparison of Figures S1g and S1h).

Figure 1a shows the comparison between D0 and D4. Whilst for a large proportion of the data (38%) the HMB does not differ (±1°), 44% of the data lie above the line of unity. For these instances the HMB is placed at a higher latitude in D4 than in D0. This is mostly prominent when the HMB for D0 is above latitudes of 59° (40% of the time). This could be due to a number of reasons, which we will discuss in Section 4. We also see a saturation of points in D0 at a HMB latitude of 60°, which is where the boundary is drawn if not enough data is available (due to low data coverage or no slow scatter being observed). The RG96 model has two boundaries where the HMB can be drawn when not enough data is available: 60° and 55°, whereas TS18 interpolates between background model solutions, so there are less discrete groupings in the HMB locations. Figure 1b shows the HMB latitude comparison between D1 and D4. Adding range limits brings the HMB distribution closer to the D4 data set, but the saturation at 60° remains, which means the HMB is most likely relying on the background fitting. This could be due to a lack of StormDARN data. Now including the PolarDARN data, Figure 1c shows the D2 data set once more moving closer to the D4 data set: The HMB moves to higher latitudes in D2 for 27% of the time. The HMB moves to higher latitudes in D2 if it cannot be defined by data in D1. For the majority of maps however (72%), the HMB does not differ at all when adding PolarDARN data. For D3 and D4, the HMB values are largely the same as the raw input data do not differ, except for times when the HMB cannot be defined. For brevity, we have chosen not to show this plot, as these cases are extremely rare (3% of cases). For D4, these cases will be defined by the background model and vary smoothly due to the interpolation in the background model between distinct bins, whereas for D3 (due to the parametrization in RG96), they will be defined as two distinct latitudes, as defined by the model: 60° (96% of instances) and 55° (4% of instances), where the 60° is the default and 55° is defined for strong, southward IMF (6 nT < | B | < 12 nT; 90° < clock angle < 270°).

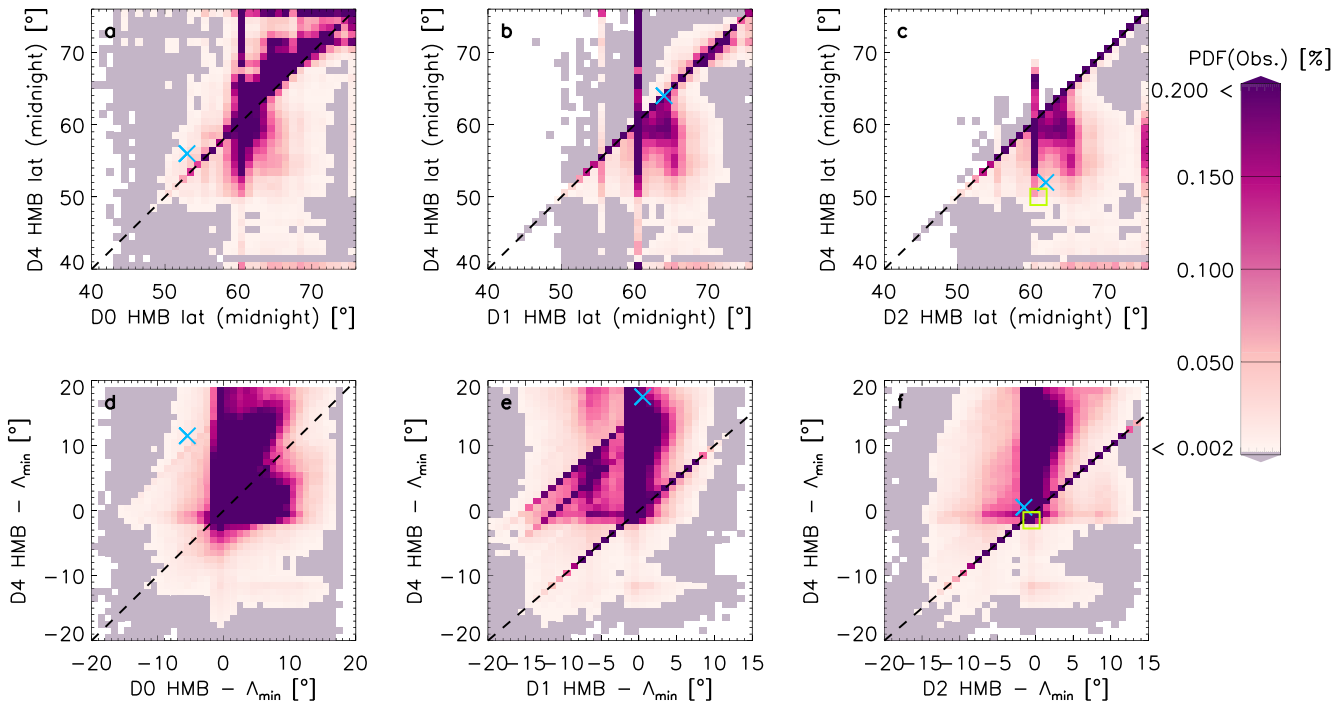

Figure 1. Probability distribution functions comparing the Heppner-Maynard boundary (HMB) latitude for (a) D0; (b) D1; (c) D2 with D4; and the difference between the HMB latitude and Λ_{min} for (d) D0; (e) D1; (f) D2 with D4. The occurrences of the example maps in Figure S1 are indicated in the PDFs by blue crosses and green square.

Figure 1d shows the difference between the HMB latitude and Λ_{min} for D0 against D4. This difference is mostly positive for both D0 and D4, which means that the HMB sits poleward of Λ_{min} and is thus well constrained. Figure 1e shows the same parameter, but comparing D1 and D4. Having added range limits, more data is in the top left quadrant of the plot than previously, where D1 is negative and D4 is positive. For these data, introducing range limits means the HMB is not well-defined in D1, but it is remedied in D4. Figure 1f shows the same parameter, but comparing D2 and D4. Adding the PolarDARN data moves a considerable proportion of these data with negative HMB-Λ_{min} and more datapoints cluster around 0, meaning that for these maps, the fitting is likely to be better constrained. It is worth noting however that even when this parameter is at 0, the HMB is not necessary bounded due to no observations being available equatorward.

3.2. Number of Backscatter Echoes

Figure 2 shows probability distribution functions for n, the number of backscatter echoes and the average n per radar.

Figure 2a shows n for D0 versus D4. Going from D0 to D4, the number of backscatter points largely increase (67% of the time), though sometimes n decreases (32% of the time), which means the introduction of range limits reduces n by more than the combined addition of Polar and StormDARN increase it by. Introducing range limits (see Figure 2b), means that for all instances, n is either higher or the same in D4 as in D1 and the same is true for D2, after the PolarDARN data have been added (see Figure 2c).

Figure 2d shows that the number of backscatter points per radar is on average higher for D0 than D4. After introducing range limits, however (Figure 2e), this is true for a slightly smaller proportion of the data. After adding the PolarDARN data (Figure 2f), we see that despite a large proportion of the data still lying below the line of unity, the gradient of the relationship has increased which means that the number of backscatter echoes per radar is higher for the StormDARN than the PolarDARN. By comparing Figures 2d–2f, we find that number of backscatter echoes per radar is lower for PolarDARN than the older radars in the network (D0 and D1).

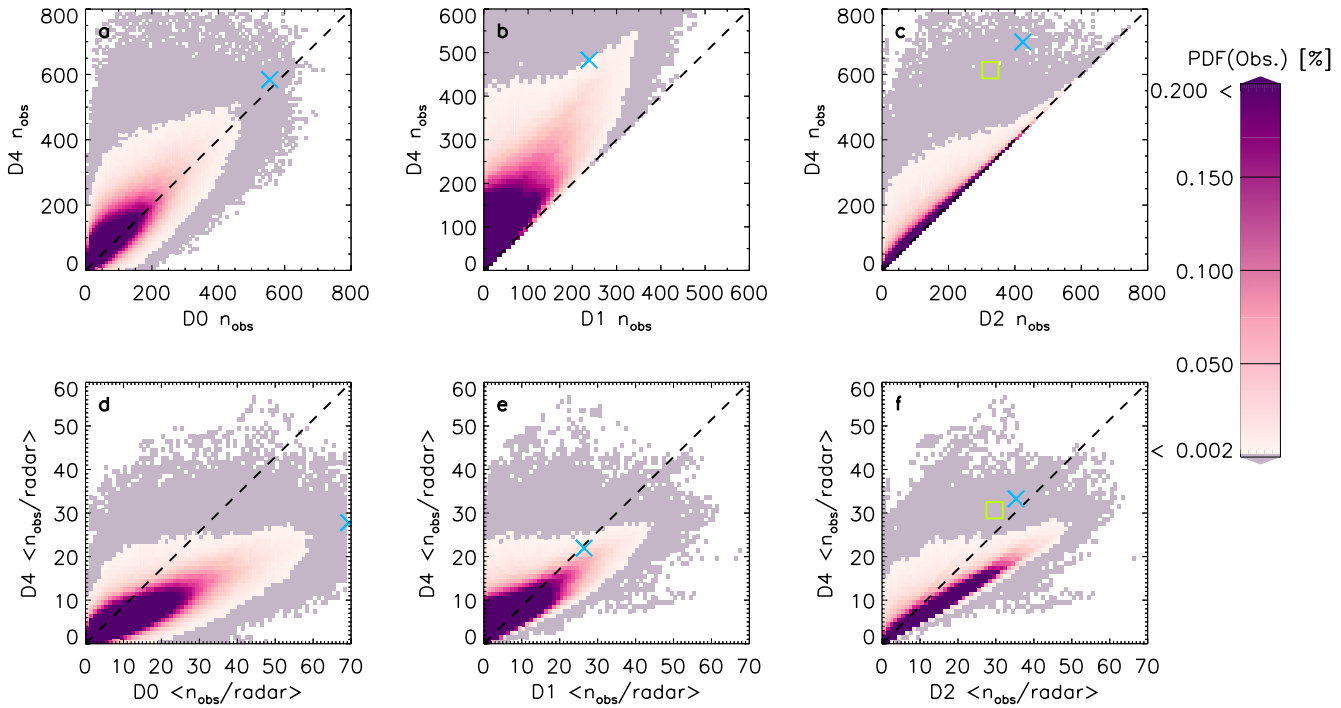

Figure 2. Probability distribution functions comparing the number of backscatter echoes for (a) D0; (b) D1; (c) D2 with D4; and the average backscatter echoes per radar for (d) D0; (e) D1; (f) D2 with D4. The occurrences of the example maps in Figure S1 are indicated in the PDFs by blue crosses and green square.

3.3. CPCP and χ^2/n

Figure 3 shows a comparison between the different datasets and D4 for the CPCP (a–d) and χ^2/n (e–h). We immediately see that the CPCP varies little on average. Figure 3a shows that the observed CPCP is on average smaller for D4 than D0 (54% of the time), but can increase or decrease from D0 to D4. When the CPCP increases (going from D0 to D4), it increases by more on average (8 kV median increase; 10 mean increase; 92 kV maximum increase; 8 kV standard deviation of the increase) than the average decrease (7 kV median decrease; 8 kV mean decrease; 98 kV maximum decrease; 5 kV standard deviation of the decrease). The increases happen however less frequently than the decreases (46% of the time, compared to the 54% of the time). We see vertical striations in the data in Figure 3a, which is due to the CPCP being discretely quantized by the RG96 model bins when the model influence is strong, whereas for TS18 interpolation between model bins occurs. Figure 3b shows the CPCP distribution for D4 and D1. Not much varies after introducing range limits, but we find that the striations are more pronounced. Comparing D1 and D4 and looking at the vertical spread, it is possible for the CPCP to increase by more than 30 kV, though the majority of data lies below the unity line and is likely to decrease by less than ~30 kV. Adding in the PolarDARN data (Figure 3c) moves the D2 CPCP closer to the D4 CPCP, but there is still some spread. We see less of the vertical striations in the CPCP for D2 than previously, which means the background model has reduced influence. Figure 3d shows the CPCP comparison between D3 and D4. After adding StormDARN data, there is little variation in the distribution in comparison to Figure 3c. At the lower range (0–~50 kV), the CPCP is likely to decrease as we change the background model from RG96 to TS18 (this occurs 42% of the time as opposed to the increase which occurs 29% of the time). For the higher range (>50 kV) however, the CPCP is likely to increase when we change model from RG96 (D3) to TS18 (D4; this occurs 16% of the time as opposed to the decrease which is 13%). Overall, TS18 thus provides a lower CPCP 55% of the time and a higher CPCP 45% of the time for the same data. The majority of data lies below the unity line and is likely to decrease by less than ~30 kV.

Figure 3e shows χ^2/n for D0 and D4. Most of the distribution lies between 1 and 10 for both datasets. We find that for the times when χ^2/n is larger in D4 than D0, n for D4 tends to small numbers (<200; 102 median; 123.13 mean). Figure 3f shows the same distribution, but for D1 and D4. Changing the data from D0 to D1, the split between increases and decreases is approximately equal (45% of χ^2/n increasing and 50% of χ^2/n decreasing).

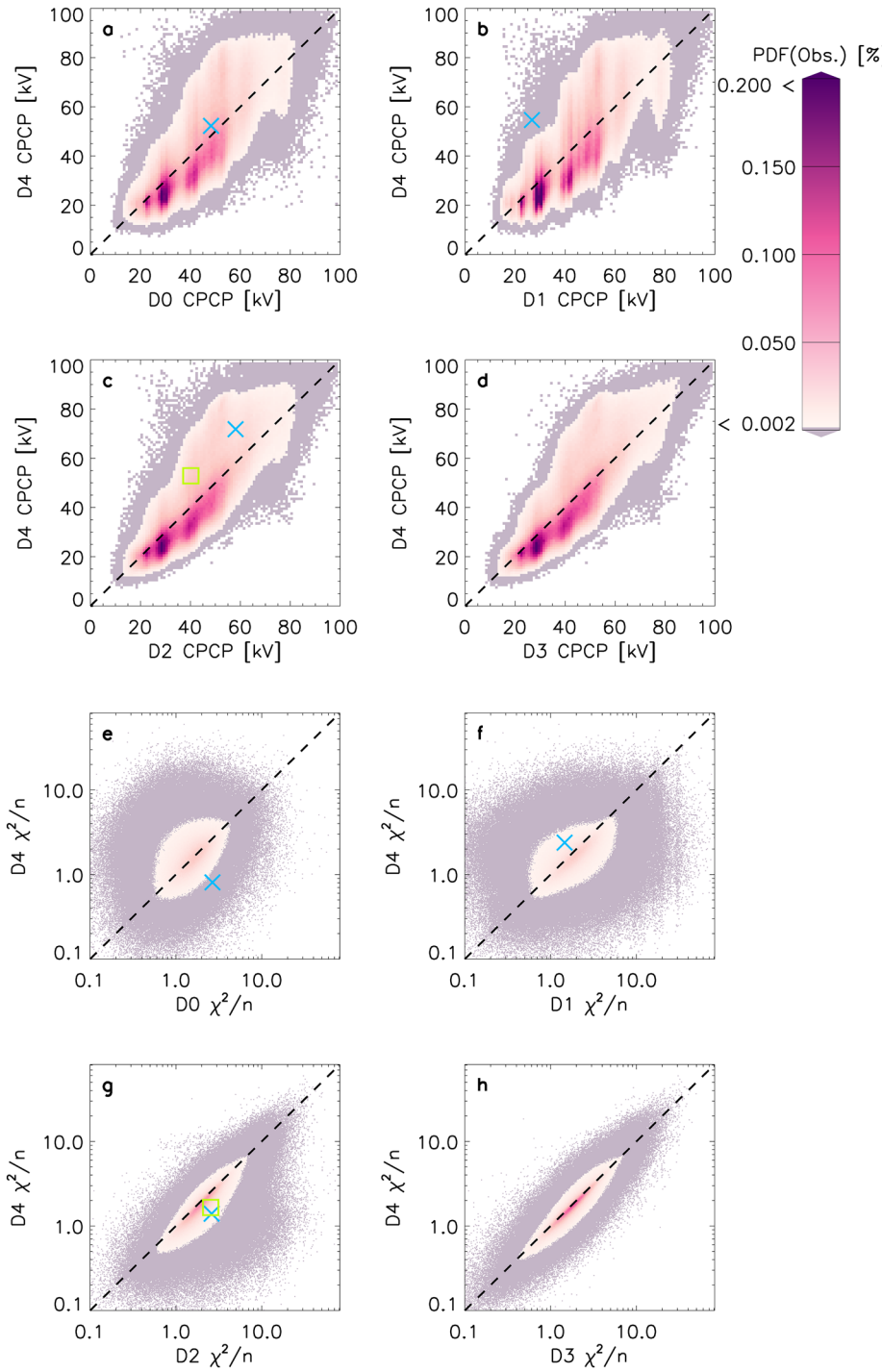

Figure 3. Probability distribution functions comparing the CPCP for (a) D0; (b) D1; (c) D2; (d) D3 with D4; and the χ^2/n distribution for (e) D0; (f) D1; (g) D2; (h) D3 with D4. The occurrences of the example maps in Figure S1 are indicated in the PDFs by blue crosses and green square.

Adding the PolarDARN data (Figure 3g), shows a slightly slimmer distribution in the *y*-direction, meaning that the parameter in D2 has moved closer to D4. The distribution moves yet closer to D4, after we add the Storm-DARN data (Figure 3h). Although not immediately obvious, 64% of the data lie below the line of unity (in comparison to 36% of data above the line) in Figure 3h, meaning the fitting error is on average reduced when making the convection maps using TS18 in comparison to RG96.

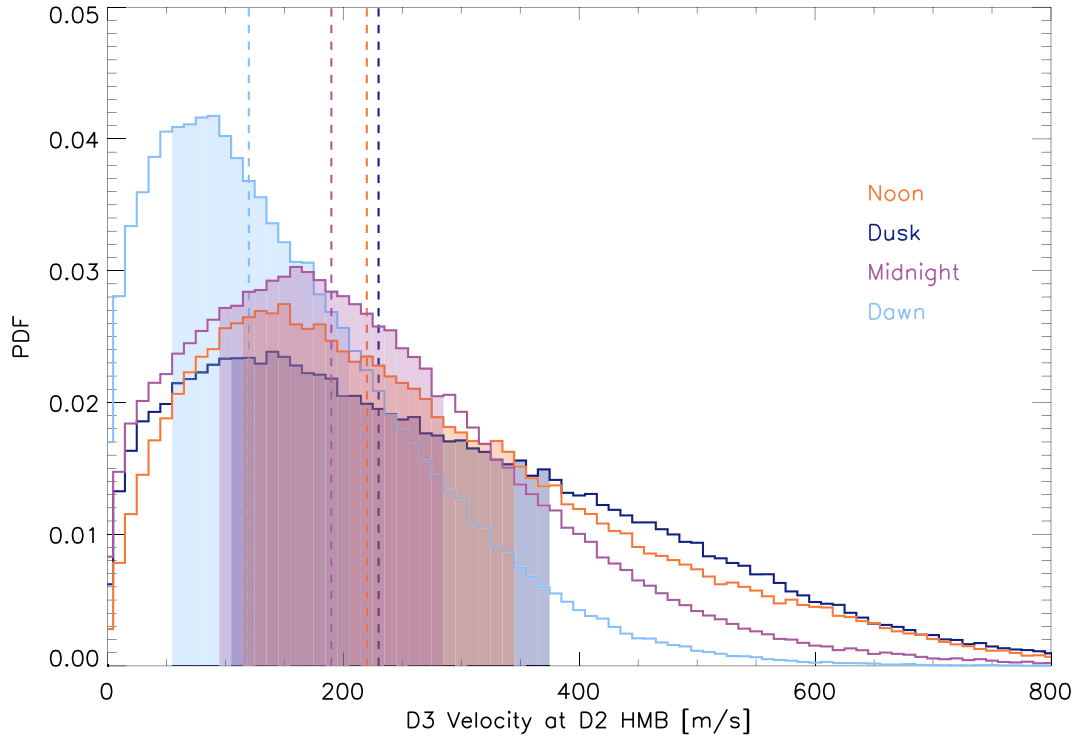

Figure 4. Probability distribution function of the velocity for D3, extracted at the noon, dusk, midnight and dawn locations where D2 would have had the Heppner-Maynard boundary (HMB). Dashed lines show the medians for each distribution. Shaded regions indicate the boundaries of the lower and upper quartiles (25% and 75%).

3.4. Differences in Velocity After Adding StormDARN

Computing the velocities for D3 at the HMB latitude location in D2 can be used as an indicator of how much the map has changed at specific locations and gives us an idea of how quantitatively different the convection maps might be without the StormDARN radars. Choosing the HMB allows us to see the maximum expected variation. We explore this in more detail now.

Figure 4 shows the velocities, extracted from the D3 convection maps for the locations where the D2-HMB intersects with the noon, dusk, midnight and dawn meridians. After adding the StormDARN data, the maps differ considerably at the locations where the HMB would have otherwise stipulated that there be zero flow. The histograms show that at dawn, the effect is the least noticeable and that there is a 1 in 2 chance that the velocity measured in D3 has increased by 120 m/s or less, whereas this increases to 190 m/s for midnight and 220 m/s and 230 m/s for noon and dusk, respectively. In 8% of cases (which equates to over 22,000 maps), adding StormDARN increases the D2-zero flow regions at midnight to >400 m/s at midnight, which indicates a considerable difference to the convection pattern.

3.5. Number of Backscatter Points in Context

We have already shown most of the differences which happen to the derived convection maps when changing the background model. Figure 5 shows further data on how changing n in D3 and D4 relates to parameters of interest (e.g., CPCP variation, HMB and Sym-H).

Figure 5a shows the CPCP difference against n. We find that the CPCP shows the least variability for maps with a high number of backscatter points, which means that there is a model dependency which decreases as n increases. For example, at $n = 200$, the median and standard deviation are 0.87 and 8.88 kV, whereas at $n = 400$, the median and standard deviation are 0.04 and 6.50 kV, respectively. The yellow crosses and error bars (which are indicative of the median and upper or lower quartiles) illustrate further that the distribution is narrowing as n increases. While using the TS18 model tends to result in a lower CPCP for less constrained maps, it can also

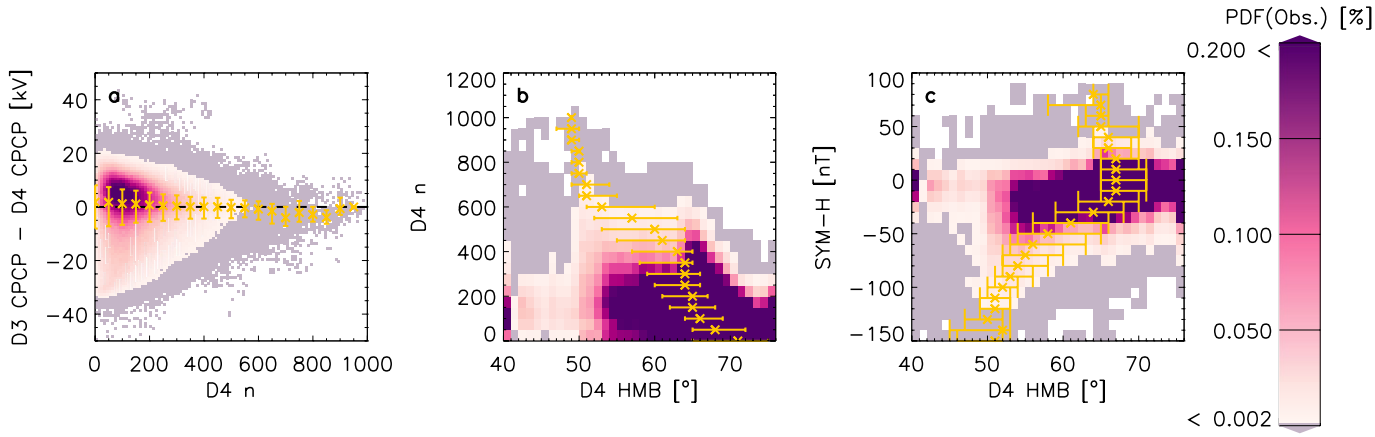

Figure 5. Probability distribution functions comparing D3 and D4 datasets: (a) cross polar cap potential (CPCP) difference versus n, (b) n versus D4 Heppner-Maynard boundary (HMB), (c) Sym-H versus D4 HMB. The black dashed line show the line at 0 and the yellow crosses show the median for the associated bins and the error bars represent the upper and lower quartiles of the distributions (75% and 25%).

overall result in a significantly larger CPCP than with RG96 Figure 5b shows the D4 HMB latitude against n. It shows that the HMB is likely to move closer to the equator as the number of backscatter echoes increases. This is again illustrated by the yellow crosses and error bars. Figure 5c shows the HMB latitude against Sym-H. There is a dependence in the HMB moving to lower latitudes as Sym-H becomes more negative. Panels (b and c) show a seemingly linear trend with HMB, which seems to break at low latitudes, but this is not supported by the yellow crosses, which show the medians for each bin.

3.6. Changes to Convection Mapping Since the Original Auroral Radars

Since the SuperDARN radar network was first built, new additions to the network have resulted in differences to the convection map data set. In this section, we compare D0 and D4 further to see this historical comparison in context. Figure 6 shows further distributions comparing D0 and D4 in the context of geomagnetic activity. Figure 6a shows the differences in the CPCP between D4 and D0 against the dayside reconnection rate, Φ_D. The differences in the CPCP tend to be smaller for high solar wind driving (high Φ_D). Similarly, Figure 6b shows the differences in the HMB against AE and Figure 6c shows the estimates in the HMB against AL. Panels (b and c) show that differences in the HMB tend to be smaller when the auroral electrojet indices, AE and AL are enhanced. Figures 6d and 6e show the D0 and D4 HMB against AL. These include yellow and blue crosses which represent the median fits for each AL bin with the error bars showing the lower (25%) and upper (75%) quartiles of the distributions, allowing us to compare D4 (yellow) with D0 (blue). This shows very clearly that when we use D0, we are less likely to observe a low HMB at enhanced (low) AL, which is not to mean that these occurrences do not exist, but simply that the SuperDARN fitting with the original data set means we are less likely to observe them. In Figures 6f and 6g, we provide a similar comparison for the D4 and D0 CPCP with respect to Φ_D. Here, we use the vertical bins to calculate the upper and lower quartiles and the medians. We show error bars for every fifth bin only due to the point density. This comparison shows that for D4 we are more likely to observe a higher CPCP at higher values of Φ_D than for D0. In fact, at a Φ_D of 100 kV, the median CPCP for D4 is at ~75 kV and ~65 kV for D0. The median curve has a different shape for the two datasets: The bulk of the distribution is at low values of solar wind driving where the median values are very similar but at higher values, the distributions differ. Both have a logarithmic shape to them and neither appear like a linear fit would suffice to describe the trend in the data set. Finally in panel (h), we show the ratio between the CPCP normalised by Φ_D for both datasets. This shows that the ratio between the two versions of the CPCP and dayside driving are proportional to each other. It also shows that these ratios increase logarithmically and that the CPCP differences with respect to Φ_D in D0 are likely to be similar to D4.

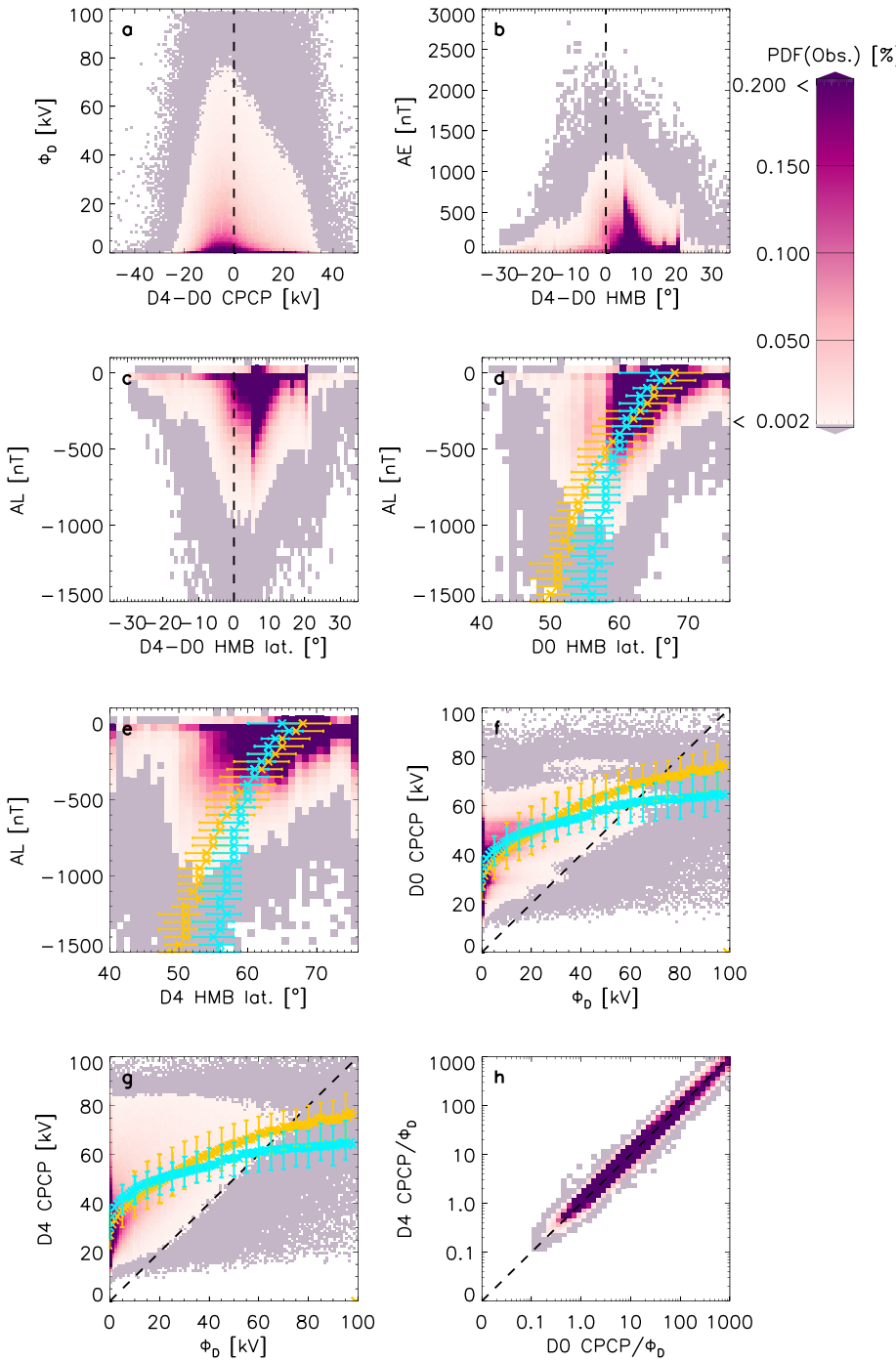

Figure 6. Probability distribution functions comparing the entire D0 and D4 datasets: (a) Φ_D versus the cross polar cap potential (CPCP) difference, (b) Auroral Electrojet (AE) versus Heppner-Maynard boundary (HMB) difference, (c) AL versus HMB difference, (d) AL versus D0 HMB and (e) D4 HMB, (f) D0 CPCP versus Φ_D, (g) D4 CPCP versus Φ_D, and (h) CPCP normalised by Φ_D. The crosses show the median in the *x*- or *y*-direction for each *y*- or x-bin (where applicable) with the yellow showing the fit for D4 and blue showing the fit for D0. Error bars represent the lower and upper quartiles of the distributions (25% and 75%, respectively). Black dashed lines either show the lines of unity or the line at 0.

3.7. Identification of Minimum Map Reliability

When using SuperDARN maps in research, a frequent question is "How reliable is this map?" and often *n* is used to answer this question. If *n* is high, the maps are often deemed more reliable, but is there a universal limit for *n*, which can be used to select reliable convection maps?

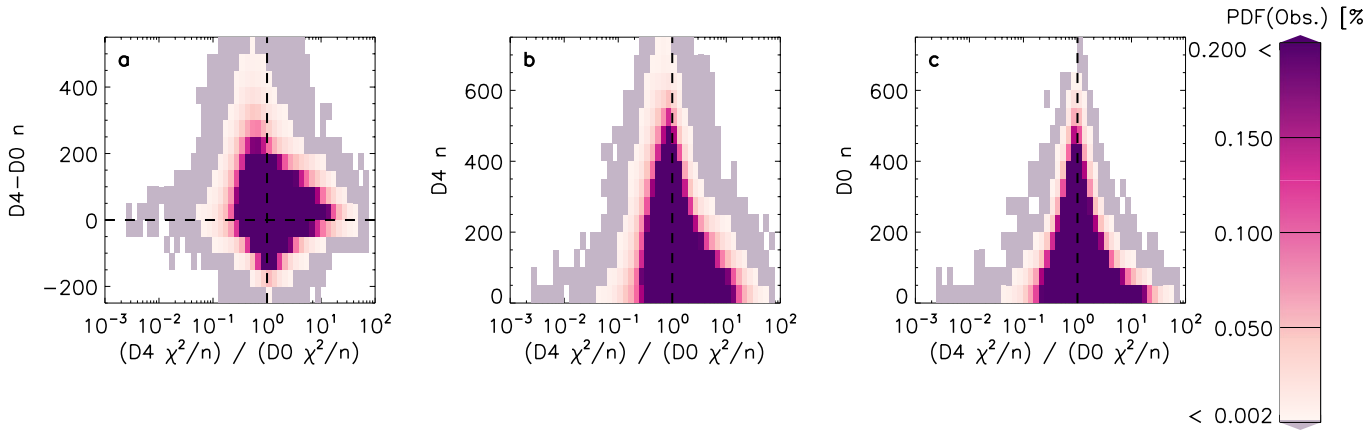

Figure 7. Probability distribution functions comparing the D0 and D4 datasets: The ratios of χ^2/n on a logarithmic scale versus (a) the differences in n, (b) D4 n and (c) D0 n. The black dashed line show the line at 0 (horizontal lines) or 1 (vertical lines).

To attempt to answer this question statistically, we present in Figure 7a the PDF of the ratio of χ^2/n between D4 and D0 on a logarithmic scale against the difference in n. It shows that as the map fitting becomes more constrained (i.e., the ratio of D4 and D0 χ^2/n comes closer to 1), the difference in n is likely to becomes smaller. As the ratio of χ^2/n becomes larger, the difference in n in also very small. This means that an increase in n does not necessarily translate to an improved map. In fact, the width of the distribution peaks in the y-direction (and differences in n are more likely to happen) for maps that are not already well constrained. Figure 7a shows that maps where χ^2/n does not differ much (i.e., ratio close to 1), the differences in n are also very small, but can also be large. Figures 7b and 7c show the ratio of the two χ^2/n on a logarithmic scale versus n in D4 and n in D0. There is a trend for χ^2/n ratio moving away from 1 as n decrease. In both D4 and D0, there is no clear uniform break-point in n, where χ^2/n ratio becomes smaller and the maps are better constrained in D4 than D0. We also find that as n increases, χ^2/n is likely to be smaller for D4 than D0, however there is less spread and the peak is more pronounced for D0 than D4. We also note that the tail in the distributions of D4 n and D0 n versus the ratio in χ^2/n are not symmetrical around 0. We will discuss these results further in the discussion section.

4. Discussion

4.1. Effect of Changing Range Limits on Derived Convection Maps

Adding range limits is intended to remove E-region scatter (i.e., scatter which moves slower than F-Region scatter), which can be assessed by direct comparison between D0-D4 and D1-D4. If we consider a simple situation where adding a range limit removes scatter moving slower than the F-region ExB velocity, then this should increase overall convection in the maps and thus the CPCP should increase. However, the blanket removal approach means that the removed scatter can also be faster than the average F-region flows, which can lead to counter-intuitive results. This will be discussed in further detail later in this section. The applied range limits also remove far-range scatter from slant range >2,000 km, which avoids potential errors in geolocation of LOS measurements at far range gates. Whilst this seems like it should constrain the spherical harmonic solution, Thomas and Shepherd (2018) have shown that the opposite is true for a data set that is limited in latitudinal coverage: Figure 11 in Thomas and Shepherd (2018) shows how range limits impacts the data coverage afforded by the high-, polar-, and mid-latitude radars. For example, when data from beyond 2,000 km slant range are removed from the high-latitude radar data set, which is comparable to our D0 to D1 variation, then the solution poleward of ∼76° magnetic latitude is purely reliant on the statistical model because no measurements are possible. This is to be expected and will be the same for our D0 to D1 comparison. Imposing the range-limit will also reduce the number of backscatter echoes in the maps but we also see that the number of backscatter echoes are not solely responsible for map quality.

Chisham and Pinnock (2002) conclude that the contamination from non-F-region scatter does not usually have a large impact on the global characteristics of the SuperDARN convection maps. However, they did show that it has

a significant effect on mesoscale features in the convection maps. Our study supports these findings in terms of the larger scale characteristics. We find that for the analyzed time period, the CPCP is >10% different 5% of the time and the CPCP is <10% different 95% of the time. Whilst less than 5% seems like a small set of observations, this does comprise more than 80,000 maps, so it may be important on a case-study basis.

Chisham and Pinnock (2002) further showed that removing E-region scatter may not always result in more accurate convection maps. Whilst most E-region scatter is believed to move slower than F-region scatter, this may not always be the case: Forsythe and Makarevich (2017) used SuperDARN data from the Southern hemisphere and showed that E-Region scatter can be of a similar order of magnitude as F-Region scatter (~200 m/s or larger). They also showed however that whilst F-Region scatter tends to have a Gaussian velocity profile, the E-Region velocity distribution is highly asymmetric, owing to the Farley-Buneman and gradient drift instabilities being the main drivers. This may be the reason why Chisham and Pinnock (2002) find that removing E-region scatter does not always improve convection maps, but the study by Forsythe and Makarevich (2017) provides clear evidence why removing this scatter makes scientific sense. Our method of adding range limits follows the strategy of Thomas and Shepherd (2018), though they used this method for statistical convection maps and this may not always be practical for instantaneous convection maps. Whilst the method employed here to remove far range backscatter is a broad-brush approach and also removes valid data, future alternatives could include the use of either calibrated elevation angles (which involves measuring the elevation angles using interferometry) or a more accurate virtual height model.

We have to consider the possibility that removing the far-range scatter reduces the integrity of the maps: The uncertainty in the geolocation of far-range scatter is expected to be of the order of ~100–200 km when using the Chisham virtual height model, which approximately equates to between one to two grid cells. Given that for an order 6 SHA fit the spatial resolution of the maps is relatively low, this level of spatial uncertainty is small.

To reduce measurement uncertainty, we remove both potential E-region scatter and scatter from far range gates. We find that by introducing range limits, the normalised Chi-squared distribution of the map fitting procedure, χ^2/n is increased 74% of the time and decreased 26% of the time.

Sometimes, reducing the number of backscatter points by introducing range limits will increase the HMB to higher latitudes due to removing lower-latitude scatter but more importantly, this difference will reduce E-region scatter at lower-latitudes and thus reduce the probability of choosing a HMB at a low latitude. For the subset of observations where this is most likely the case (i.e., the difference between the HMB and $\Lambda_{\min}$ are greater in D0 than in D1 and the HMB is at a lower latitude in D0 than in D1), the median n is higher (D0: 128 and D1: 56) than the median for the entire data set (D0: 93 and D1: 40). Other portions of the data set which may indicate a worse fitting contain the population where χ^2/n increases: here, the median n is less (D0: 86 and D1: 38) than the medians for the entire data set (D0: 93 and D1: 40). Both these statistics suggest, that n is not a good predictor for how good the fit is once range limits have been introduced if χ^2/n is used as a quality-of-fit indicator. Alternatively, we suggest that this illustrates a problem with χ^2/n and that it may not be the perfect indicator for quality. We propose that in the future, a better measure for map quality is sought. Further work is required to decide what this may be and is also necessary to evaluate which range limits would be the best choice for creating convection maps.

4.2. Effect of PolarDARN Radars on Derived Convection Maps

Adding PolarDARN to the data set increases the coverage, so we would expect the CPCP to be better constrained and n to increase.

We find that adding the PolarDARN radars decreases the CPCP on average, which could indicate that the CPCP is overestimated without good polar cap coverage or that adding PolarDARN causes an underestimation. The latter has also been shown by Mori et al. (2012), who compared the velocity measurements from PolarDARN radars to CADI ionosonde measurements, as well as comparing the CPCP. Adding range limits to our processing will remove any slow-moving E-Region scatter, which may increase the CPCP. Without polar cap measurements, it is more likely that the CPCP is estimated inaccurately, which is illustrated by the example maps in Figure S1 (c and d).

We also find that the difference between the HMB and Λ_{min} either stays the same or tends to increase when the polar radars are added to the data set. Whilst we would expect PolarDARN measurements mostly to be poleward

of the observations from the original high-latitude radars (particularly after introducing range limits), this does not seem to be the case, which is most likely due to the limited local time observations in the original (D0) maps. We also find that the HMB tends to stay the same or move poleward when adding the polar radars. This indicates that for a number of maps, the HMB was not well defined as we would not expect the introduction of PolarDARN data to move the HMB at all. While this indicates that the HMB was not always necessarily well constrained prior to the introduction of the PolarDARN data, it also indicates that observations near the pole are important when producing the maps.

Adding the PolarDARN radars to the data set can increase or decrease χ^2/n. This parameter only tends to increase for D2 if it was low for D1 and tends to decrease for D2 if it is also high for D1. This suggests that the maps where the fitting is not particularly good for D1, improve when adding PolarDARN data, but there are also a number of maps where this fitting parameter decreases. Overall however, we find that the difference between the HMB and Λ_{min} has a tendency to increase, which means the HMB is constrained by data at a lower latitude. The median n increases from 40 to 108 when adding the PolarDARN radars, which is a considerable increase in scatter.

4.3. Effect of StormDARN on Derived Convection Maps

Adding StormDARN radars improves the coverage of data at lower latitudes, we expect the HMB to move equatorward and the CPCP to be better estimated.

We find that the StormDARN radars add less data to the maps (on average), than the polar or high latitude radars, but nevertheless, adding their data to the maps generally improves the map quality. χ^2/n almost always decreases and the HMB tends to be better estimated. Adding StormDARN data tends to add low velocity scatter in lower turbulence regions, which better constrains the spherical harmonic expansion and leading to the decrease in χ^2/n.

Thomas and Shepherd (2018) made a new background model and showed that introducing the StormDARN radars could increase the CPCP by as much as 40% (for the most strongly southward IMF conditions) due to the high-latitude radars only being able to image a proportion of the convection zone necessary to estimate the CPCP. It is worth noting that Thomas and Shepherd (2018) found very little difference in the CPCP for weak to moderate solar wind driving because the low-latitude convection boundary remained within the FOV of the high-latitude radars. We find that, without using the TS18 model, but by simply including the StormDARN radars, the CPCP does indeed increase more often (12% of times) than decrease (8% of times) but the maximum difference seen is a 45% decrease when the CPCP varies from 34.70 kV in D2 to 19.19 kV in D3.

By investigating the D3 velocity measured at the HMB location of D2, we find that for 33% of cases the velocity variation is less than 200 m/s, but for a considerable number of maps (8%, which equates to over 22,000 maps), the velocity variation is >400 m/s at midnight, which indicates a considerable variation to the convection pattern. This means that without the StormDARN radars, the velocities at Λ_{HMB2} could have an uncertainty of more than 190 m/s over half the time at midnight, which is considerable, assuming the HMB placement is constrained by data.

However, we have to consider the possibility that the HMB placing is not always as good as we would like: Many convection maps from the post-StormDARN era (such as the map shown in Figure S1h, for example) show large amounts of low velocity mid-latitude convection in the nightside ionosphere, which does not seem to improve the convection map. We postulate that these streams are associated with magnetic flux frozen into the plasmasphere (the inner part of the magnetosphere located just above the ionosphere; Ribeiro et al., 2012). As the plasmasphere corotates with Earth, radars should not measure Doppler velocities associated with the rotation due to their fixed geographic location. However, if this co-rotation is not perfectly in sync with Earth's rotation then it may be possible to measure low Doppler velocities (tens-hundreds of ms^{-1}). While more transient in nature, over- or under-shielding scenarios may also lead to uncertainties in the HMB latitude determination when including the StormDARN radar data (e.g., Nishida, 1968; Nishitani et al., 2019): When this happens, the electric field formed at the inner edge of the plasma sheet and associated with the region 2 field-aligned currents counteracts the effects of the solar wind-driven magnetospheric convection at sub-auroral latitudes. Whilst these scenarios may lead to uncertainty of the HMB placement, they are understood to be exceptional circumstances and not well enough understood to be explicitly taken into account when determining the HMB (Nishitani et al., 2019). Furthermore, it is important to keep in mind that the HMB is a boundary condition, introduced to facilitate the fitting process and may in reality be different to our simplified circular shape.

4.4. Effect of Changing the Background Model on Derived Convection Maps

When changing the background model from RG96 to TS18 we might expect a more realistic fit due to a background model parametrization with more variables. The TS18 model not only uses the IMF magnetic field strength and direction, but this model parametrization also includes the solar wind's electric field and the Earth's dipole tilt, which results in 120 model bins that are trilinearly interpolated between to achieve smoother transitions, as opposed to the rigid 24 model bins chosen by RG96. The χ^2/n distribution indicates that sometimes this expected improvement is the case, however sometimes the fitting is worse (i.e., χ^2/n increases), which is primarily the case for low n maps. Overall, we find (in Figures 3 and 5) that the largest differences in the CPCP are produced when the CPCP was already high in D3 and these tend to occur when n is low. In fact, a higher n, means smaller likelihood of observing a difference in CPCP. Thomas and Shepherd (2018) compared the statistical averages over a ∼7 year period and found that the CPCP can differ by as much as 40%, when StormDARN radars are included in the convection model, which is equivalent to a difference of 32 kV for a CPCP of 80 kV without the StormDARN radars. In comparison, this study compares individual 2-min maps over a similar ∼7 year period and shows that when using this model, the maximum observed percentage difference in the CPCP is however a much larger difference: a reduction of 63% for a CPCP across this study of 49 kV in D3, which reduces to 18 kV in D4. The largest increases we find in CPCP when going from D3 to D4 is 57 kV, which happens for a CPCP of 33 kV in D3 and is a smaller difference than the smallest decrease (44 kV), which happens for a CPCP of 78 kV in D3.

Figures 5 and 6 show that both AL and Sym-H show a linear trend in the likelihood of observations with HMB: As the HMB tends to lower latitudes, the values in AL and Sym-H tend to be enhanced until the HMB reaches a latitude of ∼50°, at which point the observational likelihood reduces drastically overall. We also find that at HMBs <50°, n is likely to be smaller in general also, which means the observations in this HMB range are less dense and less well constrained. This is not surprising, as not all radars are capable of measuring HMBs <50°. Furthermore, the coverage from radars at mid-latitudes is sparser as the radars tend to, on average, return less backscatter per radar than the higher latitude radars.

We also explored how adding the newest radars to the data set, affects the convection maps (D0 to D4 comparison). This shows that the HMB is more likely to be found at lower latitudes (50°–40°) for D4 due to the lower observational latitude limit of the data. This means that the HMB is more likely to be observed at lower latitudes when the auroral electrojet indices (AL and AE) are enhanced. It is possible that the observational peak in AL and HMB, which shifts from ∼−400 nT in D0 to ∼−300 nT in D4 and ∼66° in D0 to ∼50° in D4, respectively, is still limited by radar coverage and it is possible that the decreasing trend we see in the median should continue (see crosses in Figures 6d and 6e). It is important to note however, that AL and AE are measured by 12 magnetometer stations and the current system which they measure may well move equatorward during times of high activity. This will mean that the values shown are an underestimate rather than a true estimate.

The RG96 model was built only using the data from the Goose Bay radar, which is located at a high-latitude and thus part of our D0 set. Whilst it is one of the oldest operating radars in the network (and thus a lot of data is available), the RG96 model was constrained in magnetic latitudes from 65° to 85° (Ruohoniemi & Greenwald, 1996). It is therefore interesting to find χ^2/n reduced, when adding the StormDARN radars. This shows that the data is important in generating the convection map files, but from comparing D3 and D4 we show that the model can also make a difference. It is however worth noting that due to its limited data ingestion, the RG96 model was not built to be used with a radar network that extends to mid-latitudes, whereas TS18 was. Regardless of the χ^2/n statistic not always decreasing for the variation from D3 to D4, the RG96 model does not account for as wide a variety of solar wind driving, dipolar tilt and latitudinal changes of the pattern and it thus makes more sense to use the TS18 model for the extended data set, especially when including data from the midlatitudes.

4.5. The Importance of Parametrizing the HMB

Much more than just flow velocities are affected by the HMB placement. The location of the HMB determines the boundary of the fitting, but if the CPCP is kept the same, the convection strength estimate will differ. Similarly, if the flows are kept the same, the CPCP will differ. Having a reliable HMB is therefore paramount to having a reliable map. We have seen variations of the HMB location of up to 35° (e.g., Figure 1) when StormDARN radar data are included. This shows that there is a great uncertainty in the placement of the HMB and good spatial coverage is paramount to ascertain the reliability of this.

In either case, the HMB may need to be redefined. Currently, the HMB is calculated to be where velocity measurements suggest the electric field is zero, however low velocity measurements associated with imperfect co-rotation will also have an associated nonzero electric field. This suggests the HMB would not give the boundary of the convective regions associated with opening and closing of magnetic flux or that the boundary presents as a gradual variation.

A further alternative to the HMB fitting could be the original fitting by Heppner and Maynard (1987), who used spacecraft passes to determine the HMB location. This parameterization not only provides a non-circular fit, but also one parametrized by Kp, so it could be used as an alternative for the HMB fitting. The planetary K-index, Kp, is a measure of global geomagnetic activity (e.g., Matzka et al., 2021, and references therein). Whilst this is one of the most extensively used indices, it is a 3 hourly index, which is a long timescale in the context of ionospheric convection. There is a reason why we do not produce convection maps at a 3-hourly cadence: ionospheric convection can and usually does differ on much shorter timescales. For example, Walach and Grocott (2019) and Walach et al. (2021) showed that during very active times, such as geomagnetic storms, ionospheric convection and in particularly the location of the HMB, varies on timescales of minutes and we thus do not advise to use a Kp parameterized HMB model. Walach and Grocott (2019) showed that during geomagnetic storms, which can also be described as extremely driven times, the HMB can move to latitudes as low as 40°, which SuperDARN radars prior to the mid-latitude expansion were not able to observe.

Fogg et al. (2020) provide an alternative fit for the HMB using AMPERE data, and show that the HMB may be placed at too low latitudes when StormDARN data are available. This might indicate that a changing HMB is not always an improvement when it moves equatorward in D3. It is however worth noting that the fitting by Fogg et al. (2020) does not include mid-latitude data and their fitting stops at 55°, so further analysis is necessary, which will be the subject of a future study.

Subauroral Polarization Streams (SAPS) are one of the main phenomenon studied with the StormDARN radars (e.g., Kunduri et al., 2017; Kunduri et al., 2018), which may also affect HMB parametrization. They consist of fast azimuthal streams, measured below auroral latitudes on the nightside (Kunduri et al., 2018). The possibility of the midlatitude radars observing either auroral flows in an expanded pattern, or sub-auroral flows in a smaller sized pattern, is an important distinction, which we have not studied in this paper but warrants further investigation. Kunduri et al. (2018) studied these flows in great detail and found that their occurrence and flow speed tends to increase with higher geomagnetic activity. To this date, SAPS have not been explicitly taken into account in the background SuperDARN models (e.g., RG96 and TS18) and it is thus likely that their effects are averaged over. We know that SAPS will occur at or near the lower latitudinal boundary of the convection patterns (e.g., Kunduri et al., 2018), but further investigation is necessary to understand how they fit in with the general convection pattern and in particular, how they affect HMB determination.

4.6. The Importance of Backscatter Echoes

Historically, n has on average increased due to the expansion of SuperDARN. Nevertheless, when we compare our most historic version of the data set (D0) with the version that includes all new radars, as well as updated processing techniques (TS18 and range limits), we show that sometimes n decreases (Figure 2a). This is thus solely due to introducing range limits. Whilst adding the newer radars to the data set can in some cases increase n by 500 or more, adding range limits can reduce n by 100. We have shown that n is an important parameter in constraining the convection pattern (e.g., HMB or CPCP): In particular, we find that if n is high, the CPCP is less likely to differ (i.e., the maps are constrained well) and the HMB is more likely to be found at lower latitudes (see Figure 5).

When using SuperDARN maps, the reliability of the map is important and often this has been tied to n. If n is high, the maps are often deemed more reliable (e.g., Imber et al., 2013 identified 200 to be a low threshold number for good convection maps but Fogg et al., 2020 chose 400 as threshold for an acceptable number of grid cells containing data and Lockwood & McWilliams, 2021 used a threshold of 255 for specifying the transpolar voltage). This raises the question of whether there is a universal threshold for n, which can be used to select reliable convection maps?

In Figures 7b and 7c, we show that when n is large, χ^2/n is unlikely to differ between the two datasets (the χ^2/n ratio tends to unity). However, in Figure 7a we also show that this ratio is closest to unity when the difference in

n between the two datasets is large (>200). This means that large differences in n between the datasets can have little impact on χ^2/n.

We see that for smaller n (<200), the map fitting is more sensitive to differences between the datasets (χ^2/n varies by a factor of up to 40). In Figure 7a, we see that when n is the same in both datasets the χ^2/n ratio can we large or small (either D0 or D4 being better constrained). In general, χ^2/n is likely to be larger in D4 than in D0 (the distributions of χ^2/n ratio are skewed toward positive values in Figures 7b and 7c).

Overall, whilst the biggest differences in χ^2/n are found only for $n < 200$, there is no clear threshold of n above which χ^2/n becomes completely insensitive to differences between the datasets, but we show that if we choose $n > 400$, χ^2/n is unlikely to differ by much and thus the map fitting is less sensitive to changes in the data set.

Figures 7b and 7c shows that the spread of observations becomes larger for small n and the χ^2/n ratio approaches 1 for higher n. This means that for high n, χ^2/n is likely to remain the same, so for small n, the maps are more likely to change when comparing D0 and D4. This could be due to a number of reasons, but we suggest one main cause: D4 includes data over a larger spatial range but for a sixth order SHA, only 49 vectors are required to constrain the fitting. This is to say that a sixth order SHA can be fully described by 49 vectors if they are spaced appropriately. As more vectors are added (e.g., from the midlatitude radars), it is likely that they are adding detail that the sixth order cannot resolve and thus χ^2/n is not changing drastically.

This study has not considered the spatial distribution of n in detail, which is likely to further influence map quality. Coverage at a range of local times and latitudes is likely to better constrain the map fitting procedure and this is something which needs to be explored further. SuperDARN map quality is inherently difficult to assess without an independent data set and the definition of quality can be different, depending on the type of scientific study (e.g., for a case study, spatial distribution may be a crucial measure of quality). Another way to understand quality is to consider quantitative error estimates. The SuperDARN assimilative mapping technique from Cousins et al. (2013) for example, readily provides uncertainty estimates on the potential at all spatial points.

4.7. Geomagnetic Conditions and SuperDARN Observations

We have shown in Figures 5 and 6 that when AL and Sym-H are enhanced, and the HMB is at lower latitudes, n tends to also be high. It is worth considering the underlying physics and how these parameters are related.

The expanding and contracting polar cap paradigm (e.g., Lockwood, 1991; Lockwood & Cowley, 1992; Milan, 2015; Siscoe & Huang, 1985; Walach et al., 2017, and references therein) requires the polar cap to increase in size when the dayside reconnection rate exceeds the nightside reconnection rate. This implies that the CPCP also increases when dayside driving is high. We have shown that this is mostly the case, although there are some deviations to this relationship, which we attribute to noise and errors in solar wind propagation. It has long been discussed whether or not the relationship between the dayside driving and the CPCP is linear and whether or not the CPCP saturates beyond a threshold (e.g., Doyle & Burke, 1983; Hill et al., 1976; Mori & Koustov, 2013; Reiff et al., 1981; Shepherd, 2007; Wygant et al., 1983, and references therein). Shepherd et al. (2002) and Shepherd (2007) discuss this in great detail and showed, using SuperDARN CPCP measurements, that during high solar wind driving (when the reconnection electric field is above 5.5 mV/m), the CPCP saturates.

Mori and Koustov (2013) talk about a SuperDARN "quantization" effect, whereby for high CPCP where the observational density is low and not all maps are well constrained. In this case, the CPCP oftentimes takes on the values of the underlying model, which are quantized bins for RG96. We see this quantization very clearly in Figures 3a–3c and to some extent in Figures 3d and 6f for RG96, but the quantization problem is solved for TS18, which interpolates between solutions of the background model. Whilst this is not the focal point of our study, we find that as Φ_D increases, the CPCP also increases. Similar to Shepherd (2007), we note that observational density is an important factor when considering the behavior of these parameters. We also find that depending on the data set used (e.g., D0 or D4), the trend and steepness of the curve varies due to observational density of high CPCP for D0 being much lower than for D4. Furthermore, we find that the spread in values is much higher than observed by Shepherd (2007), which is due to a larger sample size (they only used equinox data for their study) and shorter sampling (they used 10 min cadence for their map files whereas we use 2 min). We suggest that using the verb "saturate" to describe the behavior of these parameters is misplaced, as even at high values of Φ_D the CPCP increases, whereas a saturation implies the gradient of the curve reaching 0.

Whilst n is high when AL, Sym-H and the HMB are enhanced, we are not suggesting that the correlation equates to a causal link. This was already discussed by Walach and Grocott (2019), who showed that the number of backscatter echoes tends to increase during geomagnetic storms (when Sym-H is enhanced), as dayside driving increases, the polar cap grows and the HMB moves to lower latitudes. Currie et al. (2016) showed however that during intense geomagnetic storms, a reduction of backscatter was observed in the Bruny Island radar in the middle- to far-ranges, and an increase in the amount of backscatter from close-ranges. Here we show statistically, that as Sym-H is enhanced, the HMB moves to lower latitudes and the number of backscatter echoes increases for mid-ranges (the far- and close- ranges were removed beyond D0 by range limits). We thus find that the relationships found by Walach and Grocott (2019) hold statistically, though a large amount of variation is observed.

Wild and Grocott (2008) conducted a study (before the availability of StormDARN radars) of regions where backscatter is lost during isolated substorms, and the progression through the phases of the substorm due to auroral absorption. They identify that backscatter reduction is greatest at ∼70°–80° magnetic latitude region between ∼19 and 03 MLT. However, Wild and Grocott (2008) also observe that the main backscatter region shifts equatorward to lower latitudes (below ∼65°) across all local times. Our results support this statistically, as we find that the StormDARN radars do on average observe more backscatter, and that the backscatter moves to lower latitudes when AL is enhanced (which is expected to be the case for substorms). We also find that this trend differs slightly for D0 and D4: due to better coverage with the StormDARN radars, the HMB for D4 moves to lower latitudes than for D0. The trend of decreasing HMB with decreasing AL is a statistical one and thus breaks at a latitudes close to ∼40° due to low observational densities.

4.8. Is χ^2/n an Adequate Measure of Map Quality?

The current most simple way to assess map quality is to look at the χ^2/n statistic. In this study we have explored χ^2/n as a way to measure the quality of the fitting to the line-of-sight data as defined in the Data and Methods section of this paper. If we sum χ^2 and divide by the sum of n for each data set D0 to D4, we obtain the following average values: $<\chi^2/n>_{D0}$: 1.70; $<\chi^2/n>_{D1}$: 2.01; $<\chi^2/n>_{D2}$: 2.16; $<\chi^2/n>_{D3}$: 1.88; and $<\chi^2/n>_{D4}$: 1.81.

From this, we might conclude that D0 has overall the highest quality maps and is closest to the "good match" criterion (a) identified by Ruohoniemi and Baker (1998), but we have shown that whilst the map fitting may be better for D0, the missing data also equates to a qualitative penalty. A map could have a χ^2/n close to 1 (i.e., a "good" fit), but only have 10 closely clustered vectors, in which case the map is unreliable. We find from the χ^2/n distributions that most of the impact on χ^2/n are provided by range limits and the addition of the StormDARN radar data. This emphasizes the importance of good spatial coverage. We also see from these statistics, that overall, the TS18 model improves map fitting.

Furthermore, at high latitudes, in the auroral zone and polar cap, fluctuations in the velocity can be greater due to increased turbulence. These velocities are more likely to fit badly with low order spherical harmonic fits (∼6) leading to larger increases in χ^2/n. Hence, the removal of far-range scatter will obviously reduce the average χ^2/n. Conversely, low velocity scatter measured in regions of lower turbulence at low latitudes fits better to the spherical harmonic expansion and will have a smaller contribution to χ^2 per scatter point (regardless of order), and so the addition of more low-latitude low-velocity data will again reduce the average χ^2/n. Consequently, an amount of low latitude scatter will have a much smaller contribution to χ^2/n than the same amount of higher latitude scatter. But an increased goodness of fit does not always mean a "better" map. There are many example maps (such as those provided in Figures S1c and S1d) in which a low χ^2/n does not always equate to a higher quality map. True quality is however difficult to appraise. In order to achieve this, one would have to define quality first, which is beyond the scope of this study. In order to truly establish map quality, we recommend the close inspection of the individual maps and comparison with independent data, where available (e.g., Walach et al., 2017).

5. Summary

We have investigated how the SuperDARN maps have changed historically by creating 5 different versions of the convection map files for a timespan of 6 years and comparing them statistically. By using different processing parameters and gradually introducing more data to the maps, we were able to investigate how the derived convection maps differ with the inclusion of

1. Backscatter range limits (as was used by Thomas & Shepherd, 2018)
2. The polar cap radars, PolarDARN
3. The mid-latitude radars, StormDARN
4. A different background model (we compare Thomas & Shepherd, 2018 and Ruohoniemi & Greenwald, 1996)

We have shown that

1. Introducing range limits does not always decrease χ^2/n,
2. n is not a good predictor for how good the fit is once range limits have been applied,
3. Once range limits have been applied the CPCP stays the same 30% of the time and the HMB stays constant most of the time (54%),
4. The addition of PolarDARN data tends to reduce the CPCP,
5. PolarDARN radars add the most data to the data set (on average), but the StormDARN radars are also important for constraining the maps,
6. When introducing StormDARN radars to the maps, the χ^2/n values tend to decrease, the HMB becomes better constrained and the CPCP tends to increase,
7. When changing the background model to TS18, the CPCP tends to decrease for lower values of the CPCP in RG96, but is more likely to increase for larger values of the CPCP in RG96. If n is however high (>400), the CPCP is less likely to differ (differences ∼<20 kV),
8. As n, AL and Sym-H all increase, the HMB tends to go to lower latitudes, which appears to be a linear trend, though a break is seen at HMB ∼50°, where the observational density drops off sharply,
9. If n is high, the CPCP is less likely to differ and the HMB is more likely to be found at lower latitudes and χ^2/n tends to differ by the least amount,
10. There is no clear break, where n universally produces good convection maps, but we show that for $n > 400$, χ^2/n is unlikely to differ by much and thus the map is well constrained.

Naturally, assessing map quality has to include a qualitative discussion and we have found that there is currently no perfect quantitative method for this assessment.

SuperDARN provides a powerful tool for assessing solar wind-magnetosphere-ionosphere coupling and studying responses to solar wind driving of the system. Due to observations being available almost all the time, and new radars having been constructed over the years, the data set now spans several decades and is well-understood. We have presented a statistical analysis, which shows that the measured parameters (such as the CPCP and HMB) differ little on average, though in some circumstances they can be highly susceptible to which processing parameters are used, as well as which radars are used when generating map files. We have shown that most of the time, parameters such as the CPCP are unlikely to change by a large amount. However, when SuperDARN maps are used for studies of specific conditions or small case studies, as a sampling bias can occur. As a result, care has to be taken when processing the data. We have found that a high number of SuperDARN backscatter echoes are particularly important when constraining maps, so it is important to include StormDARN data in the generation of SuperDARN convection maps. The variety of conditions that we see in our statistical comparison illustrates how rich the SuperDARN data set is. Furthermore, we have illustrated concepts which can be improved. For example, we have also shown that χ^2/n is not an adequate measure of map quality and whilst the HMB is largely well-defined, the method can still be improved. Further work is thus necessary to evaluate convection map quality and generate a robust HMB selection method, especially at lower latitudes.

Appendix A: SuperDARN Processing Parameters

In the SuperDARN processing (see Section 2), we use the following parameters and functions from RST:

1. For fitting the autocorrelation function to the raw data: “make_fit” with the option “-fitacf-version 2.5.”
2. To make the gridded map files, the options “-i 120 -tl 120 -chisham -c” were added to “make_grid.”
3. To add the range limits to the gridded files, the same options as above were used but in addition, the options “-minsrng 800 -maxsrng 2,000” were added.

4. The function "map_grd" was used with "map_addhmb -vel 100 -cnt 3." Adding these options to "map_addhmb" chooses the Heppner-Maynard boundary to the lowest possible latitude for which a minimum of three LOS vectors with velocities greater than 100 m/s lie along its boundary.
5. To make the convection maps, we also use "map_addimf -if" with the text file containing the IMF data and the option "-df" with the text file containing the IMF delay times.
6. We then use "map_addmodel -o 6 " for a sixth order expansion and use "-d" to specify a light doping level.
7. Finally, we add the model option "-rg96" to D0-D3 and "-ts18" to D4 and use the function "map_fit" to make the convection map files.
8. We also use the function "cnvmaptomap" to convert the binary file to ASCII format and "trim_map" with the options "-st," "-et," "-sd," and "-ed" to make 2-hr long map files for our archive, but this is not necessary to obtain the results for this study.

Data Availability Statement

All data used for this study are available open-source from nonprofit organizations. The authors acknowledge the use of SuperDARN data. SuperDARN is a collection of radars funded by national scientific funding agencies of Australia, Canada, China, France, Italy, Japan, Norway, South Africa, United Kingdom, and United States of America, and we thank the international PI team for providing the data. The authors acknowledge access to the SuperDARN database via the British Antarctic Survey (https://www.bas.ac.uk/project/superdarn/#data). Other data mirrors are hosted by the Virginia Tech SuperDARN group (http://vt.superdarn.org/) and the University of Saskatchewan (https://superdarn.ca/data-download). The Radar Software Toolkit (RST) to process the SuperDARN data can be downloaded from Zenodo (https://doi.org/10.5281/zenodo.1403226 and references). All solar wind data and geomagnetic indices were downloaded from NASA's SPDF Coordinated Data Analysis Web (https://cdaweb.gsfc.nasa.gov/index.html/). The AE data are also available from the WDC for Geomagnetism, Kyoto (http://wdc.kugi.kyoto-u.ac.jp/wdc/Sec3.html) who prepared this index. The processed data used to make the figures in this paper are available via the (Walach, 2022).

Acknowledgments

M.-T. Walach and A. Grocott were supported by Natural Environments Research Council (NERC), UK, grant nos. NE/P001556/1 and NE/T000937/1. F. Staples was supported by a Science and Technology Funding Council (STFC) studentship. E. G. Thomas thanks the National Science Foundation (NSF) for support under grants AGS-1934997 and OPP-1836426. The authors gratefully acknowledge the use of Lancaster University's High End Computing Cluster, which has facilitated the necessary dataprocessing for this study. M.-T. Walach would like to thank LU's Women's Network Writing Group for providing a supportive virtual writing space and mentorship, which helped to forge this paper. M.-T. Walach also thanks Gareth Chisham and Mark Lester for the discussions, which helped improve this paper.

References

Chisham, G., Lester, M., Milan, S. E., Freeman, M. P., Bristow, W. A., Grocott, A., et al. (2007). A decade of the super dual auroral radar network (SuperDARN): Scientific achievements, new techniques and future directions. *Surveys in Geophysics*, *28*(1), 33–109. https://doi.org/10.1007/s10712-007-9017-8

Chisham, G., & Pinnock, M. (2002). Assessing the contamination of SuperDARN global convection maps by non-F-region backscatter. *Annales Geophysicae*, *20*(1), 13–28. https://doi.org/10.5194/angeo-20-13-2002

Chisham, G., Yeoman, T. K., & Sofko, G. J. (2008). Mapping ionospheric backscatter measured by the SuperDARN HF radars – Part 1: A new empirical virtual height model. *Annales Geophysicae*, *26*(4), 823–841. https://doi.org/10.5194/angeo-26-823-2008

Cousins, E. D. P., Matsuo, T., & Richmond, A. D. (2013). SuperDARN assimilative mapping. *Journal of Geophysical Research: Space Physics*, *118*(12), 7954–7962. https://doi.org/10.1002/2013JA019321

Cousins, E. D. P., & Shepherd, S. G. (2010). A dynamical model of high-latitude convection derived from SuperDARN plasma drift measurements. *Journal of Geophysical Research: Space Physics*, *115*(A12). https://doi.org/10.1029/2010JA016017

Currie, J. L., Waters, C. L., Menk, F. W., Sciffer, M. D., & Bristow, W. A. (2016). SuperDARN backscatter during intense geomagnetic storms. *Radio Science*, *51*(6), 814–825. https://doi.org/10.1002/2016RS005960

Davis, T. N., & Sugiura, M. (1966). Auroral electrojet activity index AE and its universal time variations. *Journal of Geophysical Research*, *71*(3), 785–801. https://doi.org/10.1029/JZ071i003p00785

Doyle, M. A., & Burke, W. J. (1983). S3-2 measurements of the polar cap potential. *Journal of Geophysical Research: Space Physics*, *88*(A11), 9125–9133. https://doi.org/10.1029/JA088iA11p09125

Fogg, A. R., Lester, M., Yeoman, T. K., Burrell, A. G., Imber, S. M., Milan, S. E., & Anderson, B. J. (2020). An improved estimation of SuperDARN Heppner-Maynard boundaries using ampere data. *Journal of Geophysical Research: Space Physics*, *125*(5), e2019JA027218. https://doi.org/10.1029/2019JA027218

Forsythe, V. V., & Makarevich, R. A. (2017). Global view of the E region irregularity and convection velocities in the high-latitude southern hemisphere. *Journal of Geophysical Research: Space Physics*, *122*(2), 2467–2483. https://doi.org/10.1002/2016JA023711

Greenwald, R. A., Baker, K. B., Dudeney, J. R., Pinnock, M., Jones, T. B., Thomas, E. C., Yamagishi, H., et al. (1995). Darn/Superdarn. *Space Science Reviews*, *71*(1–4), 761–796. https://doi.org/10.1007/BF00751350

Heppner, J. P., & Maynard, N. C. (1987). Empirical high-latitude electric field models. *Journal of Geophysical Research*, *92*(A5), 4467. https://doi.org/10.1029/JA092iA05p04467

Hill, T. W., Dessler, A. J., & Wolf, R. A. (1976). Mercury and mars: The role of ionospheric conductivity in the acceleration of magnetospheric particles. *Geophysical Research Letters*, *3*(8), 429–432. https://doi.org/10.1029/GL003i008p00429

Imber, S. M., Milan, S. E., & Lester, M. (2013). The Heppner-Maynard boundary measured by SuperDARN as a proxy for the latitude of the auroral oval. *Journal of Geophysical Research: Space Physics*, *118*(2), 685–697. https://doi.org/10.1029/2012JA018222

Iyemori, T. (1990). Storm-time magnetospheric currents inferred from mid-latitude geomagnetic field variations. *Journal of Geomagnetism and Geoelectricity*, *42*(11), 1249–1265. https://doi.org/10.5636/jgg.42.1249

Khan, H., & Cowley, S. W. H. (1999). Observations of the response time of high-latitude ionospheric convection to variations in the interplanetary magnetic field using EISCAT and IMP-8 data. *Annales Geophysicae*, *17*(10), 1306–1335. https://doi.org/10.1007/s00585-999-1306-8

Kunduri, B. S. R., Baker, J. B. H., Ruohoniemi, J. M., Nishitani, N., Oksavik, K., Erickson, P. J., & Miller, E. S. (2018). A new empirical model of the subauroral polarization stream. *Journal of Geophysical Research: Space Physics*, *123*(9), 7342–7357. https://doi.org/10.1029/2018JA025690

Kunduri, B. S. R., Baker, J. B. H., Ruohoniemi, J. M., Thomas, E. G., Shepherd, S. G., & Sterne, K. T. (2017). Statistical characterization of the large-scale structure of the subauroral polarization stream. *Journal of Geophysical Research: Space Physics*, *122*(6), 6035–6048. https://doi.org/10.1002/2017JA024131

Lockwood, M. (1991). On flow reversal boundaries and transpolar voltage in average models of high-latitude convection. *Planetary and Space Science*, *39*(3), 397–409. https://doi.org/10.1016/0032-0633(91)90002-r

Lockwood, M., & Cowley, S. W. H. (1992). Ionospheric convection and the substorm cycle. In *International conference on substorms* (pp. 99–109).

Lockwood, M., & McWilliams, K. A. (2021). A survey of 25 years' transpolar voltage data from the SuperDARN radar network and the expanding-contracting polar cap model. *Journal of Geophysical Research: Space Physics*, *126*(9), e2021JA029554. https://doi.org/10.1029/2021JA029554

Matzka, J., Stolle, C., Yamazaki, Y., Bronkalla, O., & Morschhauser, A. (2021). The geomagnetic Kp index and derived indices of geomagnetic activity. *Space Weather*, *19*(5), e2020SW002641. https://doi.org/10.1029/2020SW002641

Milan, S. E. (2015). Magnetospheric plasma physics: The impact of Jim Dungey's research. In D. Southwood, S. W. H. Cowley FRS, & S. Mitton (Eds.), *Magnetospheric plasma physics: The impact of Jim Dungey's research* (pp. 1–271). https://doi.org/10.1007/978-3-319-18359-6_2

Milan, S. E., Gosling, J. S., & Hubert, B. (2012). Relationship between interplanetary parameters and the magnetopause reconnection rate quantified from observations of the expanding polar cap. *Journal of Geophysical Research: Space Physics*, *117*(A3), A03226. https://doi.org/10.1029/2011JA017082

Mori, D., & Koustov, A. (2013). Superdarn cross polar cap potential dependence on the solar wind conditions and comparisons with models. *Advances in Space Research*, *52*(6), 1155–1167. https://doi.org/10.1016/j.asr.2013.06.019

Mori, D., Koustov, A. V., Jayachandran, P. T., & Nishitani, N. (2012). Resolute bay cadi ionosonde drifts, polardarn HF velocities, and cross polar cap potential. *Radio Science*, *47*(3). https://doi.org/10.1029/2011RS004947

Nishida, A. (1968). Coherence of geomagnetic DP 2 fluctuations with interplanetary magnetic variations. *Journal of Geophysical Research*, *73*(17), 5549–5559. https://doi.org/10.1029/JA073i017p05549

Nishitani, N., Ruohoniemi, J. M., Lester, M., Baker, J. B. H., Koustov, A. V., Shepherd, S. G., & Kikuchi, T. (2019). Review of the accomplishments of mid-latitude super dual auroral radar network (SuperDARN) HF radars. *Progress in Earth and Planetary Science*, *6*(1), 27. https://doi.org/10.1186/s40645-019-0270-5

Pettigrew, E. D., Shepherd, S. G., & Ruohoniemi, J. M. (2010). Climatological patterns of high-latitude convection in the northern and southern hemispheres: Dipole tilt dependencies and interhemispheric comparisons. *Journal of Geophysical Research: Space Physics*, *115*(A7). https://doi.org/10.1029/2009JA014956

Press, W. H., Teukolsky, S. A., Vetterling, W. T., & Flannery, B. P. (2007). *Numerical recipes: The art of scientific computing*. Cambridge University Press.

Reiff, P. H., Spiro, R. W., & Hill, T. W. (1981). Dependence of polar cap potential drop on interplanetary parameters. *Journal of Geophysical Research: Space Physics*, *86*(A9), 7639–7648. https://doi.org/10.1029/JA086iA09p07639

Ribeiro, A. J., Ruohoniemi, J. M., Baker, J. B. H., Clausen, L. B. N., Greenwald, R. A., & Lester, M. (2012). A survey of plasma irregularities as seen by the midlatitude Blackstone SuperDARN radar. *Journal of Geophysical Research: Space Physics*, *117*(A2). https://doi.org/10.1029/2011JA017207

Ruohoniemi, J. M., & Baker, K. B. (1998). Large-scale imaging of high-latitude convection with super Dual Auroral Radar Network HF radar observations. *Journal of Geophysical Research: Space Physics*, *103*(A9), 20797–20811. https://doi.org/10.1029/98JA01288

Ruohoniemi, J. M., & Greenwald, R. A. (1996). Statistical patterns of high-latitude convection obtained from Goose Bay HF radar observations. *Journal of Geophysical Research: Space Physics*, *101*(A10), 21743–21763. https://doi.org/10.1029/96JA01584

Ruohoniemi, J. M., & Greenwald, R. A. (2005). Dependencies of high-latitude plasma convection: Consideration of interplanetary magnetic field, seasonal, and universal time factors in statistical patterns. *Journal of Geophysical Research: Space Physics*, *110*, A09204. https://doi.org/10.1029/2004JA010815

Shepherd, S. G. (2007). Polar cap potential saturation: Observations, theory, and modeling. *Journal of Atmospheric and Solar-Terrestrial Physics*, *69*(3), 234–248. https://doi.org/10.1016/j.jastp.2006.07.022

Shepherd, S. G. (2014). Altitude-adjusted corrected geomagnetic coordinates: Definition and functional approximations. *Journal of Geophysical Research: Space Physics*, *119*(9), 7501–7521. https://doi.org/10.1002/2014JA020264

Shepherd, S. G., Greenwald, R. A., & Ruohoniemi, J. M. (2002). Cross polar cap potentials measured with Super Dual Auroral Radar Network during quasi-steady solar wind and interplanetary magnetic field conditions. *Journal of Geophysical Research*, *107*(A7). https://doi.org/10.1029/2001JA000152

Shepherd, S. G., & Ruohoniemi, J. M. (2000). Electrostatic potential patterns in the high-latitude ionosphere constrained by SuperDARN measurements. *Journal of Geophysical Research: Space Physics*, *105*(A10), 23005–23014. https://doi.org/10.1029/2000JA000171

Siscoe, G. L., & Huang, T. S. (1985). Polar cap inflation and deflation. *Journal of Geophysical Research*, *90*(A1), 543–547.

SuperDARN Data Analysis Working Group, Thomas, E. G., Ponomarenko, P. V., Billett, D. D., Bland, E. C., Burrell, A. G., & Walach, M.-T. (2018). Superdarn radar software toolkit (RST) (Version 4.2) [Software]. Zenodo. https://doi.org/10.5281/zenodo.1403226

SuperDARN Data Analysis Working Group, Thomas, E. G., Ponomarenko, P. V., Bland, E. C., Burrell, A. G., Kotyk, K., et al. (2018). SuperD-ARN radar software toolkit (RST) (Version 4.1) [Software]. Zenodo. https://doi.org/10.5281/zenodo.1143675

SuperDARN Data Analysis Working Group, Thomas, E. G., Sterne, K. T., Shepherd, S. G., Kotyk, K., Schmidt, M. T., Ponomarenko, P. V., et al. (2019). In Superdarn radar software toolkit (RST) (Version 4.3) [Software]. Zenodo. https://doi.org/10.5281/zenodo.3401622

Thomas, E. G., & Shepherd, S. G. (2018). Statistical patterns of ionospheric convection derived from mid-latitude, high-latitude, and polar SuperDARN HF radar observations. *Journal of Geophysical Research: Space Physics*, *123*(4), 3196–3216. https://doi.org/10.1002/2018JA025280

Walach, M. (2022). Data from Super Dual Auroral Radar Network Expansion and its Influence on the Derived Ionospheric Convection Pattern [Dataset]. Lancaster University. https://doi.org/10.17635/lancaster/researchdata/503

Walach, M.-T., & Grocott, A. (2019). Superdarn observations during geomagnetic storms, geomagnetically active times, and enhanced solar wind driving. *Journal of Geophysical Research: Space Physics*, *124*(7), 5828–5847. https://doi.org/10.1029/2019JA026816

Walach, M.-T., Grocott, A., & Milan, S. E. (2021). Average ionospheric electric field morphologies during geomagnetic storm phases. *Journal of Geophysical Research: Space Physics*, *126*(4), e2020JA028512. https://doi.org/10.1029/2020JA028512

Walach, M.-T., Milan, S. E., Yeoman, T. K., Hubert, B. A., & Hairston, M. R. (2017). Testing nowcasts of the ionospheric convection from the expanding and contracting polar cap model. *Space Weather*, *15*(4), 623–636. https://doi.org/10.1002/2017SW001615

Wild, J. A., & Grocott, A. (2008). The influence of magnetospheric substorms on SuperDARN radar backscatter. *Journal of Geophysical Research: Space Physics*, *113*(A4). https://doi.org/10.1029/2007JA012910

World Data Center for Geomagnetism in Kyoto, Nose, M., Iyemori, T., Sugiura, M., & Kamei, T. (2015). *Geomagnetic AE index*. https://doi.org/10.17593/15031-54800

Wygant, J. R., Torbert, R. B., & Mozer, F. S. (1983). Comparison of S3-3 polar cap potential drops with the interplanetary magnetic field and models of magnetopause reconnection. *Journal of Geophysical Research*, *88*(A7), 5727. https://doi.org/10.1029/JA088iA07p05727